

A Small-Scale Investigation of Molecular Emission toward the Tip of the Western Lobe of W50/SS 433

Qian-Cheng Liu¹; Yang Chen^{1,2,4}; Ping Zhou^{3,1}; Xiao Zhang¹; Bing Jiang¹

¹*Department of Astronomy, Nanjing University, 163 Xianlin Avenue, Nanjing 210023, China*

²*Key Laboratory of Modern Astronomy and Astrophysics, Nanjing University, Ministry of Education, Nanjing 210023, China*

³*Anton Pannekoek Institute, University of Amsterdam, PO Box 94249, 1090 GE Amsterdam, The Netherlands*

⁴ *Corresponding author; ygchen@nju.edu.cn*

ABSTRACT

We perform a molecular (CO and CN) line observation using IRAM 30m telescope toward two small regions near the western edge of supernova remnant (SNR) W50/SS 433. CO observation reveals spatial correspondence of two molecular clumps at the local-standard-of-rest (LSR) velocity around $+53 \text{ km s}^{-1}$ with multiwavelength local features of W50/SS 433 system. One of the two clumps appears to be embedded in a void of diffuse radio and X-ray emission. Toward the two clumps, asymmetric broad line profiles of the ^{12}CO lines are obtained, which provide kinematic evidence of the association between the clumps and the jet-related gas. The ^{12}CO $J=2-1/J=1-0$ line ratios ($\gtrsim 0.9$) and the kinetic temperatures ($\sim 30 \text{ K}$) of the clumps are distinctively higher than all those of the clumps at other LSR velocities along the same line of sight, which may be physical signatures of the association. We show that the clump coincident with the void can survive the thermal heating if it is surrounded by hot gas, with an evaporation timescale much larger than the age of SNR W50. We also show that the thermal equilibrium in the high temperature clumps can be maintained by the heating of the penetrating environmental CRs. CN ($J = 3/1-1/2$) line emission is detected in the two clumps, and the CN abundances derived are much higher than that in the interstellar molecular clouds (MCs) and that in the SNR-interacting MCs.

Subject headings: ISM: individual objects (W50 = G39.7–2.0) – ISM: supernova remnants – ISM: molecules – ISM: jets and outflows

1. Introduction

Microquasar SS 433 is the first discovered binary system containing a stellar-mass compact object with relativistic jets (Abell & Margon 1979; Fabian & Rees 1979). It is located in the center of radio shell W50, a manatee-like supernova remnant (SNR) catalogued as SNR G39.7-2.0 (Green 2014), of which the radio size is $\sim 120' \times 60'$. The W50/SS 433 system is suggested to interact with interstellar medium (ISM; e.g., Huang et al. 1983; Wang et al. 1990; Dubner et al. 1998; Durouchoux et al. 2000; Lockman et al. 2007; Yamamoto et al. 2008; Su et al. 2018) and induce the molecular clouds (MCs) formation (e.g., Yamamoto et al. 2008; Asahina et al. 2014; Su et al. 2018). Except for the W50/SS 433 system, there is very few observational example in our Galaxy for the possible association between relativistic jet and MC (e.g., Furukawa et al. 2014). In a larger scale, active galactic nucleus radio jet feedback could have important impact on the ISM of the host galaxy and affect the process of star formation. However, it is yet unclear how the molecular gas is affected by the jet. Hence, the study of the microquasar in our Galaxy, like the SS 433/W50 system, toward which possible association with MC has been suggested, could provide an opportunity for a detailed, deep case study of this kind of physical process.

The jet on each side of SS 433 is extended by $\sim 1^\circ$ (Kotani 1998), an angular size which can be translated to a length of about 50–80 pc at an estimated distance of $\sim 3\text{--}5$ kpc (e.g., Hjellming & Johnston 1981; Dubner et al. 1998; Blundell & Bowler 2004; Yamamoto et al. 2008; Marshall et al. 2013; Panferov 2014; Shan et al. 2018; Su et al. 2018). In radio band, the large-scale environment of W50 has been studied (e.g., Geldzahler et al. 1980; Downes et al. 1981, 1986; Dubner et al. 1998; Gao et al. 2011), and the radio ears of W50 were suggested to be the result of the interaction between the ram pressure of the jets and the SNR shell (e.g., Elston & Baum 1987). In far-infrared (IR), six knots were found (Band 1987; Band & Gordon 1989), and suggested to be a result of jet-clump interaction (Wang et al. 1990). In X-rays, two bright, diffuse lobes were found (Watson et al. 1983), and the possible interaction between the jets and its ambient gas have been studied using data from ROSAT, ASCA, RXTE, and Chandra (Yamauchi et al. 1994; Brinkmann et al. 1996; Safi-Harb & Ögelman 1997; Safi-Harb & Petre 1999; Moldowan et al. 2005; Brinkmann et al. 2007). In gamma-rays, emissions have been detected by the *Fermi* Large Area Telescope (LAT; e.g., Bordas et al. 2015) toward SS 433, by the High Altitude Water Cherenkov observatory (Abeysekara et al. 2018) toward the lobes of SS 433, and no evidence of gamma-ray emission from the jet termination regions have been found between a few hundred GeV and a few TeV (MAGIC Collaboration et al. 2018).

W50 was suggested to lie at the end of a filamentary MC at local-standard-of-rest (LSR) velocity $V_{\text{LSR}} \sim +32 \text{ km s}^{-1}$ and be related to the MC (Huang et al. 1983). A scenario of

SNR-HI interaction at $V_{\text{LSR}} \sim +42 \text{ km s}^{-1}$ was suggested according to the observation of radio continuum emission at 1.4 GHz and emission of HI 21 cm (Dubner et al. 1998). An MC at $V_{\text{LSR}} \sim +50 \text{ km s}^{-1}$ was found to be spatially coincident with the X-ray hot spots toward one part of the jets (Durouchoux et al. 2000). The shapes of two MCs at $V_{\text{LSR}} \sim +50 \text{ km s}^{-1}$ were found to be similar to the $15\mu\text{m}$ mid-IR emission shape (Fuchs 2002). Furthermore, ten MCs were found at $V_{\text{LSR}} = +40 - +60 \text{ km s}^{-1}$, which align nearly along the axis of the jets of SS 433 based on an analysis of the NANTEN ^{12}CO ($J=1-0$) data (Yamamoto et al. 2008). Accordingly, they are suggested to be created by the interaction between the relativistic jets and the ambient interstellar HI gas. However, the low spatial resolution ($2''.6$) and grid spacing ($4''$) of the data used in the paper prevented the study of the kinematic/physical features of the clumps. In addition, H^{13}CO^+ molecules was found at the western part of the W50/SS 433 system at $V_{\text{LSR}} = +50 - +55 \text{ km s}^{-1}$ (Chaty et al. 2001). Nonetheless, it is also argued that the system is associated with the gas material at LSR velocity of $\sim +75 \text{ km s}^{-1}$ according to observations of HI, CO and optical emission (Boumis et al. 2007; Lockman et al. 2007; Su et al. 2018).

The interaction between jet and ISM has also been studied by hydrodynamic and magnetohydrodynamic (MHD) simulations, and it is shown that MCs can be formed (e.g., Asahina et al. 2014, 2017) with either arc-like shape or a line-like shape that align with the jet, depending on the filling factor of the HI clumps that the jet interacts with (Asahina et al. 2017). Although the assumed velocities of the jets in the simulations (about hundreds km s^{-1}) are much smaller than that for SS 433 ($\sim 0.26 c$; Margon & Anderson 1989), these results have demonstrated that the jets of SS 433 do have a potential to induce MC formation, especially when penetrating into dense HI environment (e.g., the western lobe of W50, which is closer to the disk of the Milky Way).

Although there are some observational results that are consistent with the scenario of interaction between molecular gas and the W50/SS 433 system (e.g., Yamamoto et al. 2008; Su et al. 2018), it is still an open question whether there is association and at which LSR velocity the association could be (Band & Gordon 1989; Dubner et al. 1998; Durouchoux et al. 2000; Chaty et al. 2001; Moldowan et al. 2005; Boumis et al. 2007; Lockman et al. 2007; Yamamoto et al. 2008; Su et al. 2018). There are a few observational evidence for judging the interaction with MCs, such as molecular line broadening, high high-to-low excitation line ratio, morphological agreement (Jiang et al. 2010; Chen et al. 2014). Motivated by the observational study of the ten molecular clumps in Yamamoto et al. (2008) and the simulational study of distribution of the molecular gas interacting with a jet (e.g., Asahina et al. 2014, 2017), we have performed an IRAM 30m observation toward two of the ten clumps (SS 433-N3 and part of SS 433-N2 in Yamamoto et al. 2008) in molecular lines. The two clumps are located at the western tip of the X-ray and radio emission which are suggested to result from

the interaction of the jet of SS 433 and the surrounding medium (e.g., Safi-Harb & Ögelman 1997; Dubner et al. 1998). The two clumps were selected based on the following two considerations: (1) They are located at the low Galactic latitude, where the HI density should be higher than at the other side, making the jet-induced CO formation to be more plausible (e.g., Asahina et al. 2017); (2) Since they are located at the tip of the radio emission, any possible morphological correspondence could be easier to be observed. In this paper, we report the CO and CN line observation toward the two clumps, aiming to look for the signature of the interaction of the W50/SS 433 system with the MCs in a higher spatial resolution. We first describe the observations of the CO line emissions and data reduction process in §2; we present the result of our CO data in detail in §3 and discuss the main result in §4. Finally, we summarize this paper in §5.

2. Observations and data reduction

Our observations of molecular lines toward SNR W50 were made simultaneously in ^{12}CO ($J=1-0$), ^{13}CO ($J=1-0$), and ^{12}CO ($J=2-1$) with the IRAM 30 m telescope during 2017 December 09–10, with a total of 12 hours. The observations covered two regions of areas $\sim 5' \times 9'$ and $\sim 12' \times 10'$ centered at $(19^{\text{h}}08^{\text{m}}10^{\text{s}}, +05^{\circ}02'45'', \text{J2000})$ and $(19^{\text{h}}08^{\text{m}}58^{\text{s}}, +05^{\circ}07'14'', \text{J2000})$ (regions N2 and N3 hereafter, corresponding to part of SS 433-N2 and complete SS 433-N3 in Yamamoto et al. 2008) respectively. The mappings were conducted with the on-the-fly position switching mode using the Eight Mixer Receiver (EMIR) in E0 and E1 bands and the fast Fourier transform spectrometers (FTS). The backend FTS provided either a bandwidth of 4 GHz and a spectral resolution of 50 kHz in part of the observation during 2017 December 09 or a bandwidth of 16 GHz and a spectral resolution of 200 kHz. Noteworthy, the emission of CN ($J=3/2-1/2$ $F=5/2-3/2$) line at 113.491 GHz, which was recognized in our analysis (see §3), was covered in the wider bandwidth of 16 GHz mode. The observational information, including the velocity resolution for each line, is summarized in Table 1 (note that the ^{13}CO ($J=1-0$) line was failed to be covered when a high velocity resolution of 0.127 km s^{-1} was applied to ^{12}CO ($J=1-0$)). The half-power beam width (HPBW) of the telescope were $\sim 21''$ at 115 GHz and $\sim 10.7''$ at 230 GHz, with main-beam efficiencies of $\sim 78\%$ at 115 GHz and $\sim 59\%$ at 230 GHz, respectively. All the data observed with IRAM 30m telescope were reduced using the GILDAS/CLASS package developed by the IRAM observatory¹. To reduce the noise level, the ^{12}CO ($J=2-1$) line data were resampled to achieve a velocity resolution 0.3 km s^{-1} , while the data of other lines (^{12}CO ($J=1-0$), ^{13}CO ($J=1-0$), and CN ($J=3/2-1/2$ $F=5/2-3/2$)) were resampled to achieve a velocity resolution

¹ <http://www.iram.fr/IRAMFR/GILDAS>

0.6 km s^{-1} . Also, the angular resolution of each line data was convolved to $22''$. The mean rms noise levels of the main-beam temperature (T_{mb}) of the data are $\sim 0.3/0.2 \text{ K}$ ($^{12}\text{CO } J=1-0$), $\sim 0.15/0.1 \text{ K}$ ($^{13}\text{CO } J=1-0$, $\text{CN } J=3/2-1/2$ $F=5/2-3/2$), and $\sim 0.23/0.19 \text{ K}$ ($^{12}\text{CO } J=2-1$) for the N2/N3 regions, respectively.

In addition, we used $^{12}\text{CO } (J=1-0)$ data from the Milky Way Imaging Scroll Painting (MWISP) project, which was observed with the 13.7 m millimeter-wavelength telescope of the Purple Mountain Observatory at Delingha (PMOD), to show the larger environment of the N2 and N3 regions. The HPBW of the data was $\sim 50''$, with velocity resolutions of $\sim 0.16 \text{ km s}^{-1}$ for ^{12}CO and $\sim 0.17 \text{ km s}^{-1}$ for ^{13}CO and C^{18}O . The typical mean rms noise levels were 0.5 K for ^{12}CO and 0.25 K for ^{13}CO and C^{18}O . For a purpose of multiwavelength investigation of the environment, we also used *ROSAT* PSPC X-ray (ObsID: US400271P-1.N1, PI: Marshall Dr., Francis E.), *WISE* 12/22 μm mid-IR (*WISE* Science Data Center, IPAC, Caltech), and VLA 1.4 GHz radio continuum (from Dubner et al. 1998) data.

3. Results

3.1. Spatial distribution of the clouds

Figure 1 shows the averaged CO spectra from regions N2 and N3 that were observed with IRAM 30m. The CO spectra of region N2 are somewhat different from N3. There are two prominent $^{12}\text{CO } (J=1-0)$ and $^{12}\text{CO } (J=2-1)$ emission peaks, at around $+8 \text{ km s}^{-1}$ and $+53 \text{ km s}^{-1}$, in region N2, while the $^{13}\text{CO } (J=1-0)$ emission is only prominent at $\sim +53 \text{ km s}^{-1}$. On the other hand, four prominent $^{12}\text{CO } (J=1-0)$ and $^{12}\text{CO } (J=2-1)$ emission peaks, at around $+8 \text{ km s}^{-1}$, $+26 \text{ km s}^{-1}$, $+53 \text{ km s}^{-1}$, and $+56 \text{ km s}^{-1}$, are shown in region N3. Only one prominent $^{13}\text{CO } (J=1-0)$ emission peak (at $\sim +53 \text{ km s}^{-1}$) can be seen in region N3. Also, the $^{12}\text{CO}(J=2-1)/(J=1-0)$ line ratios are higher at $\sim +53 \text{ km s}^{-1}$ than at other velocity ranges in both regions N2 and N3.

We made $^{12}\text{CO } (J=1-0)$ emission channel maps around each velocity component to examine the spatial distribution of those molecular clumps. No clear morphological correspondence between molecular clouds and the SNR was found for CO clumps at velocities below $+40 \text{ km s}^{-1}$, which is consistent with the results in Su et al. (2018). The $^{12}\text{CO } (J=1-0)$ and $^{13}\text{CO } (J=1-0)$ emission channel maps of the $\sim +53 \text{ km s}^{-1}$ clumps in regions N2 and N3, with velocity interval 0.6 km s^{-1} , are shown in Figure 2 and Figure 3. Some spatial features related to the clumps and the surrounding multiwavelength emission are noteworthy.

- (1) Region N2: (a) Globally, it lies outside of the western tip of the radio continuum.
- (b) In velocity interval $+53.8 - +54.4 \text{ km s}^{-1}$, there is a weak arc-like structure in ^{12}CO

($J=1-0$) emission channel maps (Figure 2). The structure, however, does not appear in the ^{13}CO ($J=1-0$) channel maps (Figure 3).

(2) Region N3: (a) There is a remarkable arc-like structure in velocity interval $\sim +51.4 - +53.2 \text{ km s}^{-1}$ (Figure 2), which can also be discerned in the ^{13}CO ($J=1-0$) channel map in velocity interval $\sim +52 - +52.6 \text{ km s}^{-1}$ (Figure 3). (b) This clump is anticorrelated with the radio continuum, appearing embedded in a void of radio emission (Figure 2 and 3), which is more clearly shown in the upper left panel of Figure 4. The clump is also anticorrelated to the radio continuum at 327.5 MHz (Dubner et al. 1998) and at 150 MHz (Broderick et al. 2018). It will be shown in § 4.1 that the clump is unlikely located in the foreground to cause the low radio brightness in region N3 by extinction. (c) This clump is located on the tip of an X-ray lobe, and the X-ray emission toward the clump is weaker than its surrounding (see the bottom left panel of Figure 4). That is, there also seems to be an anticorrelation between the clump and the X-ray emission.

(3) Mid-IR view: Although there is a lot of IR emission in the field, which makes the analysis of the IR emission to be complicated, it is noteworthy that the clumps at $\sim +53 \text{ km s}^{-1}$ in both regions N2 and N3 are essentially spatially correlated with two patches of enhanced mid-IR emission (see upper right panel of Figure 4). Since the IR emission at $\sim 12 \mu\text{m}$ seems to be dominated by aromatic molecules (e.g., Verstraete et al. 2001; Wang & Chen 2010) apart from possibly unignorable contribution from warm dust, the correlation between the IR emission and the clumps in regions N2 and N3 may indicate dense gas there. The mid-IR emission (in a square root scale), on the other hand, finely encloses the western edge of the X-ray lobe (especially the patch along the northwestern edge), with an anti-correlated brightness distribution with each other (see bottom right panel of Figure 4). This seems to imply that the dense gas indicated by the $+53 \text{ km s}^{-1}$ clumps and the mid-IR emission is associated with the western X-ray and radio lobe.

In addition to the two clumps described above, there is another molecular clump in region N1 south to the tip of the western lobe (as shown in Figure 4), which is identical to the clump named as “SS433-N1” in Yamamoto et al. (2008). Three clumps in regions N1, N2, and N3 are all located near the tip of the lobe. Such an arc-like spatial distribution of molecular gas seems somewhat similar to the simulational result with large filling factor of HI clumps (Asahina et al. 2017).

3.2. Molecular line profiles

We have inspected the CO line profiles toward N2 and N3. For clumps with $V_{\text{LSR}} < +40 \text{ km s}^{-1}$, neither asymmetric broad line profile of the ^{12}CO ($J=1-0$) nor high ^{12}CO $J=2-1/J=1-0$ line ratio has been found. For clumps around $+53 \text{ km s}^{-1}$, we made grids of ^{12}CO ($J=1-0$), ^{12}CO ($J=2-1$), and ^{13}CO ($J=1-0$) spectra in the velocity range $+47 - +61 \text{ km s}^{-1}$ and $+49 - +61 \text{ km s}^{-1}$ (part of N2 and N3 are shown in Figure 5 and Figure 6, respectively). There are some common characteristics of the spectra of the clumps in regions N2 and N3.

(1) The kinetic temperatures $T_{\text{c,k}}$ estimated from the peak of the main-beam temperatures can reach 28/30 K for N2/N3 (see Table 2), which are significantly higher than all those ($\sim 10 \text{ K}$, similar to the typical temperature for interstellar MCs) at other LSR velocities (see Figure 7 for a comparison with the clumps at $\sim +26 \text{ km s}^{-1}$ and $\sim +8 \text{ km s}^{-1}$). Here we consider that $T_{\text{c,k}}$ is equal to the excitation temperature T_{ex} under the assumption of local thermodynamic equilibrium (LTE). T_{ex} is calculated from the main-beam temperature T_{mb} using the equations $T_{\text{ex}} = 5.53 / \{\ln[1 + 5.53 / (T_{\text{mb},10} + 0.84)]\} \text{ K}$ for ^{12}CO ($J=1-0$) and $T_{\text{ex}} = 11.06 / \{\ln[1 + 11.06 / (T_{\text{mb},21} + 0.2)]\} \text{ K}$ for ^{12}CO ($J=2-1$).

(2) The ^{12}CO $J=2-1/J=1-0$ line ratios, $R_{21/10} = T_{\text{MB},21}/T_{\text{MB},10}$, of the clumps are high. The $R_{21/10}$ maps and the 1σ error maps for the LSR velocity intervals $+50 - +60 \text{ km s}^{-1}$, $+24 - +28 \text{ km s}^{-1}$, and $+6 - +10 \text{ km s}^{-1}$ are shown in Figure 8. It is seen that the line ratios are > 0.9 for most part of the clumps at $\sim +53 \text{ km s}^{-1}$. As a comparison, the ratios for the clumps at $\sim +26 \text{ km s}^{-1}$ and $\sim +8 \text{ km s}^{-1}$ are $\lesssim 0.8$ (see the middle-left and bottom-left panels in Figure 8).

(3) Both N2 and N3 show some asymmetric broad profiles of the ^{12}CO line. Figure 9 shows the average line profiles delineated by the green rectangles labeled with “2” and “3” in Figure 5 and 6. As is shown, the red (right) wings of the ^{12}CO lines appear to be broadened at $\sim +54 - +59 \text{ km s}^{-1}$ and $\sim +56 - +59 \text{ km s}^{-1}$ for regions “2” and “3”, respectively. The one-side widths $\sim 5 \text{ km s}^{-1}$ and $\sim 3 \text{ km s}^{-1}$ of the broad right (red) wings are notably larger than the half-widths of the FWHMs ($\sim 1.5 \text{ km s}^{-1}$ and $\sim 0.9 \text{ km s}^{-1}$, Table 2) of the main bodies of the velocity components, respectively. There is no sign that these line wings could be contamination from their surrounding pixels, somewhat similar to the ^{12}CO spectra detected in the southwestern edge of SNR CTB 87 (Liu et al. 2018). That is, there are strong peaks at $\sim +53 \text{ km s}^{-1} / \sim +55 \text{ km s}^{-1}$ for both ^{12}CO and ^{13}CO in regions “2”/“3”, while the broad red wings of ^{12}CO extending to $+59 \text{ km s}^{-1}$ without significant ^{13}CO counterparts, and further their surroundings are weak in the velocity range where the ^{12}CO red wings are. Such asymmetric/one-sided broadened ^{12}CO line profiles are present in many SNR-MC interaction systems, like Kes 75 (Su et al. 2009), 3C 397 (Jiang et al. 2010), Kes 78 (Zhou & Chen 2011), 3C 396 (Su et al. 2011), and CTB 87 (Liu et al. 2018). Usually,

the asymmetric part deviating from the main Gaussian in a ^{12}CO profile is believed to be a broadened part if there is little ^{13}CO line feature at the corresponding LSR velocity. Because ^{13}CO emission, whose optical depth is smaller than 1 in most cases (i.e., optically thin, which is satisfied in this work, as is given in Table 2), traces the quiescent gas, the lack of significant ^{13}CO feature at the velocity indicates that the deviating part is very likely to represent the disturbed gas due to external interaction (e.g., Su et al. 2011; Zhou & Chen 2011; Zhou et al. 2016). Therefore, the broad ^{12}CO red wings from regions “2” and “3” are highly likely to result from Doppler broadening of the $\sim +53 \text{ km s}^{-1}/\sim +55 \text{ km s}^{-1}$ lines and thus could represent a kinematic signature of the perturbation of the $\sim +53 \text{ km s}^{-1}/\sim +55 \text{ km s}^{-1}$ MC clumps by external impacts, especially from the jet-related gas.

Table 2 summarizes the observed and derived parameters for the two clumps in regions N2 and N3 as observed in the three CO lines at $+50 - +60 \text{ km s}^{-1}$. We then estimated the distribution of the column density $N(\text{H}_2)$ using ^{13}CO lines, under the assumption of LTE for the MCs, optically thick condition for the ^{12}CO ($J=1-0$) line, and optically thin condition for the ^{13}CO ($J=1-0$) line. The excitation temperature of the two clumps, are assumed to be $T_{\text{ex}} = 28 \text{ K}$ for N2 and $T_{\text{ex}} = 31 \text{ K}$ for N3 (see Table 2). Here we have used the conversion relation for the molecular column density of $N(\text{H}_2) \approx 7 \times 10^5 N(^{13}\text{CO})$ (Frerking et al. 1982). The estimated $N(\text{H}_2)$ distribution at $+50 - +60 \text{ km s}^{-1}$ is shown in Figure 10, with maximum values of $\sim 2.3 \times 10^{22} \text{ cm}^{-2}$ in N2 and $\sim 1.2 \times 10^{22} \text{ cm}^{-2}$ in N3 (however, it is noticeable that the column density could be overestimated by a factor of up to 4 with the ^{13}CO , see Wilson et al. 2013). The H_2 masses and mean H_2 densities in the field-of-view are also estimated and summarized in Table 2, when parameterizing the distance to the MC as $d = 3.5 d_{3.5} \text{ kpc}$ (Yamamoto et al. 2008).

3.3. Emission lines of CN at $+50 - +58 \text{ km s}^{-1}$

We detected emission lines of CN ($J=3/2-1/2$) at six small regions (labeled with white crosses in the upper left panel of Figure 4, with each of only several pixels). The CN emission at $+50 - +58 \text{ km s}^{-1}$ could arise from denser part of the MCs with density of order 10^5 cm^{-3} (Turner & Gammon 1975), which is much higher than the average densities of the two clumps estimated from the CO lines (of order 10^3 cm^{-3} , see Table 2). The position information and the size of the six regions are summarized in Table 3. Figure 11 shows the CN ($J=3/2-1/2$ $F=5/2-3/2$) spectra from the six regions.

Though there are five CN ($N=1-0$, $J=3/2-1/2$) hyperfine splitting lines in frequency 113.488–113.521 GHz range, we suggest the CN line we observed in this work to be the CN ($J=3/2-1/2$ $F=5/2-3/2$) hyperfine line based on the observational result that the CN line

we observed coincident with the CO spectra quite well in velocity interval $+50$ – $+60$ km s^{-1} (see Figure 11) if we set the reference frequency to be CN ($J=3/2-1/2$ $F=5/2-3/2$) of 113.491 GHz. Also, the CN ($J=3/2-1/2$ $F=5/2-3/2$) has the strongest relative intensity among the hyperfine lines (Turner & Gammon 1975). The second strongest hyperfine line, CN ($J=3/2-1/2$, $F=3/2-1/2$) at 113.488 GHz, which is ~ 7 km s^{-1} away from the CN ($J=3/2-1/2$ $F=5/2-3/2$), has not been detected within the noise level.

The column densities of CN are estimated with radiative transfer calculations of the CN ($J=3/2-1/2$ $F=5/2-3/2$) lines using the RADEX code under the LVG approximation (van der Tak et al. 2007). The input parameters, including the kinetic temperature, the line width, and the brightness temperature, are taken as the estimated excitation temperature of N2 and N3 (see Table 2), the maximum CN ($J=3/2-1/2$ $F=5/2-3/2$) emission point, the fitted FWHM of the CN ($J=3/2-1/2$ $F=5/2-3/2$) emission line, respectively. The best-fitting results of the CN column densities are shown in Table 3.

In Table 3, we also list the column densities of $N(\text{H}_2)$ and the CN abundances, $N(\text{CN})/N(\text{H}_2)$, toward each position where the CN emission is detected. The CN abundances are in a range ~ 1 – 6×10^{-8} , which are about an order of magnitude higher than that in the interstellar MC (e.g., Blake et al. 1987; Watanabe et al. 2014) and that in the MC an SNR interacts with (e.g., Turner et al. 1992). The derived CN abundances are consistent with the abundance (~ 1.4 – 4.1×10^{-8}) estimated for an MC which interacts with CRs in timescales of 10^4 – 10^5 yr (Albertsson et al. 2018).

4. Discussion

Our small-scale CO-line observation shows that the two clumps at LSR velocity around $+53$ km s^{-1} near the tip of the western lobe of the SS 433/W50 system are spatially correspondent with multiwavelength local features of the system. Toward the two clumps, asymmetric broad line profiles of the ^{12}CO lines are obtained, which provide kinematic evidence of the association between the clumps and the jet-related gas. The ^{12}CO $J=2-1/J=1-0$ line ratios ($\gtrsim 0.9$), as well as the kinetic temperatures (~ 30 K), of the two clumps are distinctively higher than all those of the MCs at other LSR velocities along the same LOS, which may be physical signatures of the association. Some physical issues in this scenario are discussed below.

4.1. The anticorrelation between the radio emission and the clump in region N3

With the properties favoring an interaction between the clumps at $\sim +53 \text{ km s}^{-1}$ and the western lobe of SS 433 (i.e., the asymmetrical ^{12}CO lines, high $^{12}\text{CO } J=2-1/J=1-0$ line ratios, and the high molecular gas temperatures) obtained, the anticorrelation between the clump in region N3 and the radio continuum (as shown in Figure 4) may unlikely be due to a chance projection effect. It could hardly result from extinction by the clump located in the foreground of SS 433, because either the electron scattering or the free-free absorption is negligible for the extinction of the radio emission. The optical depth of electron scattering can be estimated as $\tau_{\text{es}} = \sigma_e n_e l$, where $\sigma_e = 6.65 \times 10^{-25} \text{ cm}^2$ is the total cross section of an electron, n_e is the electron density ($\sim 0.05 \text{ cm}^{-3}$) for a clump with a density of $\sim 10^3 \text{ cm}^{-3}$ (Table 2) and a CR ionization rate of $\zeta(\text{H}_2) \sim 5 \times 10^{-16} \text{ s}^{-1}$ (see §4.3) and l ($\sim 1 \text{ pc}$) is the length of the clump along the line of sight (LOS). We thus have $\tau_{\text{es}} \sim 1 \times 10^{-7} \ll 1$. The optical depth of free-free absorption by electron can be expressed as $\tau_{\text{ff}} = k_\nu l$, where $k_\nu = 0.1731[1 + 0.13 \log(T_{\text{c,k}}^{3/2}/\nu)](Z^2 n_e n_i)/(T_{\text{c,k}}^{3/2} \nu^2) \text{ cm}^{-1}$ (Spitzer 1978), in which Z is the charge of ions (~ 1), n_i is the ion density (very similar to n_e). The optical depth of free-free absorption can thus be estimated to be $\tau_{\text{ff}} \sim 3 \times 10^{-7} \ll 1$ for $T_{\text{c,k}} \sim 30 \text{ K}$ and $\nu = 1.4 \text{ GHz}$. Therefore, the anticorrelation between the CO emission and the radio continuum is not caused by the molecular gas extinction, similar to the case in SNR CTB 109 (e.g., Tatematsu et al. 1987; Wang et al. 1992). It hence suggests a scenario that the clump in region N3 could be embedded in the radio emitting gas in the western lobe of SS 433.

4.2. Evaporation of the clump

We have indicated that the clump in region N3 may be embedded in the western lobe. This scenario is consistent with the location of this clump which projectively seems to be in a void of X-ray emission (§ 3.1). If it implies that the clump is surrounded by the X-ray emitting hot gas of the western lobe, the clump seems to survive the heating of the gas.

In the case that the X-rays of the lobe is dominated by thermal bremsstrahlung, the gas temperature is $\sim 3.3 \text{ keV}$ or $\sim 4 \times 10^7 \text{ K}$ (Safi-Harb & Ögelman 1997). For simplicity, we only estimate the evaporative effect on the clump due to saturated thermal conduction from the hot gas. As a result of heating on the clump surface by inward heat flux from the high-temperature, low-density environment, the cold clump could gradually evaporate (Cowie & McKee 1977). It is essential to compare the evaporation timescale of the clump in N3 with the age of the SS 433 system. The saturated mass loss rate is given by $\dot{m} =$

$3.25 \times 10^{18} n_h T_h^{1/2} R_{\text{pc}}^2 \phi F(\sigma_0) \text{g s}^{-1}$ (Cowie & McKee 1977), where n_h and T_h are the atomic density and temperature for the hot medium, where R_{pc} is the radius of the clump in unit of pc, ϕ is a factor of order unity to equate the saturated heat flux and the pressure of the medium times the isothermal sound speed, and $F(\sigma_0)$ is a function with a value ~ 8 for σ_0 , the saturation parameter, around ~ 20 under the physical condition of the hot gas considered here. The evaporation timescale of the clump in region N3 can be estimated as:

$$\tau_{\text{ev}} \sim M/\dot{m} \sim 8 \times 10^5 d_{3.5}^2 R_{\text{pc}}^{-2} \phi^{-1} \left(\frac{n_h}{0.3 \text{ cm}^{-3}} \right)^{-1} \left(\frac{T_h}{4 \times 10^7 \text{ K}} \right)^{-1/2} \left(\frac{F(\sigma_0)}{8} \right)^{-1} \text{ yr}, \quad (1)$$

where M is the mass of the clump ($\sim 500 d_{3.5}^2 M_\odot$ for that in N3; Table 2), and a number density $n_h \sim 0.3 \text{ cm}^{-3}$ given in the thermal bremsstrahlung model (Safi-Harb & Ögelman 1997) is adopted as a reference value. By contrast, it is suggested that the age of SNR W50 is $\sim 10^5 \text{ yr}$ and the age of the SS 433 jets is $< 2.7 \times 10^4 \text{ yr}$ (Panferov 2017), both of which are much smaller than the evaporation timescale. This means that evaporation of the cold gas is far from exhausting the embedded clump.

4.3. The heating source of the clumps

The $^{12}\text{CO } J=2-1/J=1-0$ line ratios are as high as 0.9–1 for the clumps in regions N2 and N3 (§ 3.2), implying that the gas temperatures of the clumps could be evidently higher than the typical temperature of interstellar molecular gas ($\sim 10 \text{ K}$). The line ratio is given by $R_{21/10} = f_{21} \nu_{21} [J_{\nu_{21}}(T_{\text{ex}}) - J_{\nu_{21}}(T_{\text{bg}})] [1 - e^{-\tau_{21}}] / \{ f_{10} \nu_{10} [J_{\nu_{10}}(T_{\text{ex}}) - J_{\nu_{10}}(T_{\text{bg}})] [1 - e^{-\tau_{10}}] \}$, where $T_{\text{MB},ji}$, f_{ji} , ν_{ji} , and τ_{ji} are the main-beam temperature, filling factor, frequency, and optical depth of the $^{12}\text{CO } J = j-i$ line emission, respectively, $J_{\nu_{ji}}(T) \equiv (e^{h\nu_{ji}/kT} - 1)^{-1}$, and $T_{\text{bg}} \sim 2.73 \text{ K}$ is the background temperature. Since the clumps are optically thick ($\tau_{ji} > 1$) and diffuse ($f_{ji} = 1$) for $^{12}\text{CO } J=2-1$ and $J=1-0$ line emission, the line ratio can be approximated as:

$$R_{21/10} \approx 2 \times [J_{\nu_{21}}(T_{\text{ex}}) - J_{\nu_{21}}(T_{\text{bg}})] / [J_{\nu_{10}}(T_{\text{ex}}) - J_{\nu_{10}}(T_{\text{bg}})], \quad (2)$$

which is $\gtrsim 0.9$ for $T_{\text{ex}} \gtrsim 20 \text{ K}$. Therefore, the line ratios observed in the two clumps appear to be consistent with the obtained kinetic temperatures (28/30 K, § 3.2). Also, such line ratio and temperature are clearly higher than all those (~ 0.8 and $\sim 10 \text{ K}$) of the molecular gas at other LSR velocities along the same LOS (see the comparisons in Figures 7 and 8). There should be heating source(s) for the clumps, with possible candidates including environmental X-rays, external disturbance, and cosmic rays (CRs). The heat flux from the surrounding hot gas is consumed by the gas evaporation on the clump surface.

The environmental diffusive X-ray emission plays an insignificant role in heating the clumps, although the X-rays could heat the molecular gas in the far-UV-shielded regions (i.e., regions beneath the surface of the MCs with column density larger than 10^{21} cm^{-2} , see, e.g., Zhou et al. 2018). Safi-Harb & Ögelman (1997) gives the X-ray luminosity of a circular region “w2”, the brightest portion in the lobe, near the clump in region N3: $L_X \lesssim 2 \times 10^{34} (d/5.5 \text{ kpc})^2 \text{ erg s}^{-1}$ in 0.1–2.4 keV. The angular radius of the circle is $\mathcal{R} = 3.75'$, which can be translated to $\mathcal{R} \sim 3.9 d_{3.5} \text{ pc}$. The X-ray flux around the sphere indicated by this circle region $F_X = L_X / (4\pi \mathcal{R}^2) \lesssim 5 \times 10^{-6} \text{ erg cm}^{-2} \text{ s}^{-1}$ is used as an upper limit of the X-ray flux at the clump in N3. The X-ray heating rate can be approximated as (Maloney et al. 1996) $\Gamma_X = 1.4 \times 10^{-26} [n(\text{H}_2)/10^3 \text{ cm}^{-3}] [F_X / (5 \times 10^{-6} \text{ erg cm}^{-2} \text{ s}^{-1})] (N_H/10^{22} \text{ cm}^{-2})^{-0.9} \text{ erg cm}^{-3} \text{ s}^{-1}$, where N_H is the column density of hydrogen attenuating the X-ray flux. On the other hand, the cooling of MCs with kinetic temperature of dozens of Kelvin and density of $\sim 10^3 \text{ cm}^{-3}$ is dominated by molecular lines, and the cooling rate can be approximated by (Goldsmith 2001) $\Lambda_{\text{gas}} \sim 1.5 \times 10^{-23} (T_{\text{c,k}}/30 \text{ K})^{2.4} [(dv/dr)/(1 \text{ km s}^{-1} \text{ pc}^{-1})] \text{ erg cm}^{-3} \text{ s}^{-1}$, where dv/dr is the velocity gradient of the MCs. The X-ray heating rate is about 3 orders of magnitude smaller than the cooling rate, indicating that the X-ray heating is actually negligible.

The obtained broadened ^{12}CO lines can be ascribed to an external disturbance, which could have a heating effect on the clumps. However, it can not play an important role in heating the clumps. The transmission velocity of the disturbance should be comparable to the redshifted ^{12}CO line broadening ($\sim 3\text{--}5 \text{ km s}^{-1}$). The timescale for the disturbance to cross the clump with a typical size $\sim 1 \text{ pc}$ is about $2\text{--}3 \times 10^5 \text{ yr}$, which is an order of magnitude larger than the age of the jets ($< 2.7 \times 10^4 \text{ yr}$, Panferov 2017).

CRs could penetrate deeply into the far-ultraviolet-shielded regions of MCs and ionize the molecules. The ionization process can provide a heating rate (Goldsmith & Langer 1978) $\Gamma_{\text{CR}} = \zeta(\text{H}_2) \Delta Q n(\text{H}_2) \sim 6.4 \times 10^{-25} [n(\text{H}_2)/10^3 \text{ cm}^{-3}] [\zeta(\text{H}_2)/(2 \times 10^{-17} \text{ s}^{-1})] \text{ erg cm}^{-3} \text{ s}^{-1}$, where $\zeta(\text{H}_2)$ is the ionization rate of H_2 by CR and ΔQ is the energy deposited as heat per ionization. Here a mean value of 20 eV is adopted for ΔQ , though it varies with CR energy and gas composition (e.g., Goldsmith & Langer 1978; Glassgold et al. 2012). To maintain a temperature $T_{\text{c,k}} \sim 30 \text{ K}$ via thermal equilibrium $\Gamma_{\text{CR}} = \Lambda_{\text{gas}}$, the ionization rate should be

$$\zeta(\text{H}_2) \sim 4.7 \times 10^{-16} \left(\frac{T_{\text{c,k}}}{30 \text{ K}} \right)^{2.4} \left(\frac{n(\text{H}_2)}{10^3 \text{ cm}^{-3}} \right)^{-1} \left(\frac{dv/dr}{1 \text{ km s}^{-1} \text{ pc}^{-1}} \right) \text{ s}^{-1}. \quad (3)$$

This rate appears somewhat larger than the background CR ionization rate ranging from $\sim 2 \times 10^{-17} \text{ s}^{-1}$ (Goldsmith & Langer 1978) to $\sim 2 \times 10^{-16} \text{ s}^{-1}$ (e.g., Indriolo & McCall 2012). It is, however, not surprising because the energy density of CRs may be expected to be higher at locations (like N3 and N2) inside or close to the boundary of an SNR (i.e., W50) and near the energetic jets than the Galactic mean.

In the scenario the two observed clumps are associated with the W50/SS 433 system, the energy expended to maintain the high molecule temperature in a timescale τ is $\Gamma_{\text{CR}}[M/\rho(\text{H}_2)]\tau$, where $\rho(\text{H}_2)$ is the mass density of the molecular gas; for the clump in N3 and adopting τ as the age of SNR W50, this energy is $\sim 1.4 \times 10^{46} (M/500 M_\odot) (T_{\text{c,k}}/30\text{K})^{2.4} [n(\text{H}_2)/(10^3 \text{cm}^{-3})]^{-1} [(dv/dr)/(1 \text{km s}^{-1} \text{pc}^{-1})] (\tau/10^5 \text{yr}) \text{erg}$. A canonical energy for the CRs accelerated by the SNR shock, about ten percent of the supernova explosion energy 10^{51}erg , together with the energy that may be potentially converted from the SS 433 jets, is a few orders of magnitude larger than the energy needed to maintain the thermal equilibrium in the clumps.

4.4. Gamma-ray emission from the clumps?

The CRs may produce considerable gamma-rays by pp interactions, a process which has also been discussed toward the central part of SS 433 (e.g., Reynoso et al. 2008). To calculate the gamma-ray flux, one needs to know the energy density (w) of CRs in the clumps, which can be estimated by scaling the ionization rate obtained in this paper to that caused by the background CRs. The ionization rate for the background CRs above 10 MeV is estimated to be $\sim 2 \times 10^{-17} \text{s}^{-1}$ (Takayanagi 1973; Goldsmith & Langer 1978). From Eq. A1 in Takayanagi (1973), we obtain the energy density of the background CRs above 1 GeV $w_0(> 1 \text{GeV}) \sim 0.4 \text{eV cm}^{-3}$. Thus, according to the ionization rate obtained, we have $w(> 1 \text{GeV}) \sim 20w_0 \sim 8 \text{eV cm}^{-3}$ as the energy density of the CRs that heat and maintain the high temperature of the molecular clumps. We further assume the CR distribution has a power-law form with a proton index α_p and a maximum energy of 3 PeV. Then the π^0 -decay gamma-ray emissivity per H-atom, $q_\gamma(E_\gamma)$, can be obtained according to the formulae given in Kafexhiu et al. (2014). The expected gamma-ray flux from the two clumps is $(M_{\text{cl}}/m_p) \times (q_\gamma(E_\gamma)/4\pi d^2)$, which is shown in Figure 12. Here, we consider two cases with different proton index: $\alpha_p = 2.0$ and $\alpha_p = 2.3$. For the both cases the gamma-ray flux estimated is lower than the sensitivity of current telescope, Fermi and HESS in GeV and TeV band, respectively, which is consistent with the report that no evidence of gamma-ray emission from the jet termination regions have been found between a few hundred GeV and a few TeV (MAGIC Collaboration et al. 2018). For $\alpha_p = 2.0$, the gamma-ray flux seems to be detectable with CTA, the next generation TeV telescope. However, if the transport of CRs to the clumps is governed by diffusion, the proton index should be $\alpha_p = \alpha'_p + \delta$, where α'_p is the proton index at the acceleration site and δ is the index of the diffusion coefficient $D(E) \propto E^\delta$. If one takes $\alpha'_p = 2.0$ as predicted by the standard diffusive shock acceleration theory and the typical value of $\delta \sim 0.3\text{--}0.7$ for the diffusion coefficient in ISM, the proton index in the clumps should be greater than 2.3. Therefore, the expected gamma-ray emissions are even

undetectable with the next generation telescope.

4.5. Clump formation?

The clumps in regions N2 and N3, as well as in N1, are all located near the tip of the western X-ray or radio lobe (§ 3.1). An MHD simulation suggests that MCs can be formed by the jet-HI clump interaction: when the filling factor of the HI clumps the jet interacts with is large, arc-like distributed MCs with thickness of ~ 1 pc are formed (Asahina et al. 2017). Compared with the observed arc-like spatial distribution of the clumps in this work, the simulation could imply that the filling factor of the HI clumps is large in the west of SS 433, under the scenario that the clumps are potentially produced by the jet-HI interaction. This is in general consistent with the environment of the clumps in the west of SS 433, where the Galactic latitude is low, and the HI gas could be dense. In addition, the high CN abundances found in some positions in the molecular clumps are consistent with model predictions of MC which interacts with CRs in timescale of 10^4 – 10^5 yr (§ 3.3). This timescale is comparable to the age of the SS 433 jet $< 2.7 \times 10^4$ yr (Panferov 2017). However, to confirm if the clumps are induced by jet-HI interaction, further investigations are needed.

5. Summary

We perform a small-scale CO-line observation using the IRAM 30m telescope toward two regions (N2 and N3) near the western tip of the X-ray and radio emission that are suggested to result from the interaction of the jet of SS 433 and the surrounding medium. The observational and physical properties of the molecular clumps in the two regions are summarized below.

1. The CO observation shows that two clumps in the two regions at around $V_{\text{LSR}} \sim +53 \text{ km s}^{-1}$ are spatially correlated with dense gas indicated by two patches of enhanced mid-IR emission. The clump in region N3 appears to be embedded in a void of diffuse radio emission, while the western edge of the X-ray emission is finely enclosed by the mid-IR emission. The negligible optical depth of the clump indicates that the radio void is unlikely due to an extinction by the clump located in the foreground
2. Asymmetric broad line profiles of the $\sim +53 \text{ km s}^{-1}$ ^{12}CO lines are obtained, which is a kinematic evidence of the association between the clumps and the jet-related gas. The $^{12}\text{CO } J=2-1/J=1-0$ line ratios ($\gtrsim 0.9$) and the kinetic temperatures ($\sim 30 \text{ K}$) of the

two clumps are distinctively higher than all those of the MCs at other LSR velocities along the same LOS, which may be physical signatures of the association.

3. We also detect emission lines of CN ($J = 3/1-1/2$) at six positions in the two clumps, and the derived CN abundances are about an order of magnitude higher than that in the interstellar MCs and that in the MCs with that SNRs interact.
4. We show that the clump in region N3 can survive the thermal heating if it is surrounded by hot gas, with the evaporation timescale much larger than the age of SNR W50. We also show that the thermal equilibrium in the high temperature clumps can be maintained by the heating of the penetrating environmental CRs.

We are grateful to Yang Su for the discussion about the W50/SS 433 environment and the MC physics. We thank the staff of IRAM 30 m observatory for the help during the observation. We acknowledge the MWISP project. This work is supported by the National Key R&D Program of China under grants 2017YFA0402600 and 2015CB857100 and the NSFC under grants 11773014, 11633007, 11851305, 11503008, 11590781, and 11203013. P.Z. acknowledges the support from the NWO Veni Fellowship, grant NO. 639.041.647. B.J. acknowledges the Jiangsu NSF grant BK20141310 and SRFDP of China 20110091120001.

REFERENCES

- Abell, G. O., & Margon, B. 1979, *Nature*, 279, 701
- Abeysekera, A. U., Albert, A., Alfaro, R., et al. 2018, *Nature*, 562, 82
- Albertsson, T., Kauffmann, J., & Menten, K. M. 2018, *ApJ*, 868, 40
- Asahina, Y., Ogawa, T., Kawashima, T., et al. 2014, *ApJ*, 789, 79
- Asahina, Y., Kawashima, T., Furukawa, N., et al. 2017, *ApJ*, 836, 213
- Band, D. L. 1987, *PASP*, 99, 1269
- Band, D. L., & Gordon, M. A. 1989, *ApJ*, 338, 945
- Blake, G. A., Sutton, E. C., Masson, C. R., et al. 1987, *ApJ*, 315, 621
- Blundell, K. M., & Bowler, M. G. 2004, *ApJ*, 616, L159
- Bordas, P., Yang, R., Kafexhiu, E., et al. 2015, *ApJ*, 807, L8

- Boumis, P., Meaburn, J., Alikakos, J., et al. 2007, MNRAS, 381, 308
- Brinkmann, W., Aschenbach, B., & Kawai, N. 1996, A&A, 312, 306
- Brinkmann, W., Pratt, G. W., Rohr, S., et al. 2007, A&A, 463, 611
- Broderick, J. W., Fender, R. P., Miller-Jones, J. C. A., et al. 2018, MNRAS, 475, 5360
- Chaty, S., Rodríguez, L. F., Mirabel, I. F., et al. 2001, A&A, 366, 1035
- Chen, Y., Jiang, B., Zhou, P., et al. 2014, Supernova Environmental Impacts, 170
- Cowie, L. L., & McKee, C. F. 1977, ApJ, 211, 135
- di Sciascio, G., & Lhaaso Collaboration 2016, Nuclear and Particle Physics Proceedings, 279-281, 166
- Downes, A. J. B., Pauls, T., & Salter, C. J. 1986, MNRAS, 218, 393
- Downes, A. J. B., Salter, C. J., & Pauls, T. 1981, A&A, 97, 296
- Dubner, G. M., Holdaway, M., Goss, W. M., & Mirabel, I. F. 1998, AJ, 116, 1842
- Durouchoux, P., Sood, R., Oka, T., et al. 2000, Advances in Space Research, 25, 703
- Elston, R., & Baum, S. 1987, AJ, 94, 1633
- Fabian, A. C., & Rees, M. J. 1979, MNRAS, 187, 13P
- Frerking, M. A., Langer, W. D., & Wilson, R. W. 1982, ApJ, 262, 590
- Fuchs, Y. 2002, arXiv e-prints, astro-ph/0207429
- Funk, S., Hinton, J. A., & CTA Consortium 2013, Astroparticle Physics, 43, 348
- Furukawa, N., Ohama, A., Fukuda, T., et al. 2014, ApJ, 781, 70
- Gao, X. Y., Han, J. L., Reich, W., et al. 2011, A&A, 529, A159
- Geldzahler, B. J., Pauls, T., & Salter, C. J. 1980, A&A, 84, 237
- Glassgold, A. E., Galli, D., & Padovani, M. 2012, ApJ, 756, 157
- Goldsmith, P. F. 2001, ApJ, 557, 736
- Goldsmith, P. F., & Langer, W. D. 1978, ApJ, 222, 881

- Green, D. A. 2014, *Bulletin of the Astronomical Society of India*, 42, 47
- Hjellming, R. M., & Johnston, K. J. 1981, *ApJ*, 246, L141
- Huang, Y.-L., Dame, T. M., & Thaddeus, P. 1983, *ApJ*, 272, 609
- Indriolo, N., & McCall, B. J. 2012, *ApJ*, 745, 91
- Jiang, B., Chen, Y., Wang, J., et al. 2010, *ApJ*, 712, 1147
- Kafexhiu, E., Aharonian, F., Taylor, A. M., et al. 2014, *Phys. Rev. D*, 90, 123014
- Kelner, S. R., Aharonian, F. A., & Bugayov, V. V. 2006, *Phys. Rev. D*, 74, 034018
- Kotani, T. 1998, Ph.D. Thesis
- Kothes, R., Reich, W., Foster, T., et al. 2003, *ApJ*, 588, 852
- Liu, Q.-C., Chen, Y., Chen, B.-Q., et al. 2018, *ApJ*, 859, 173
- Lockman, F. J., Blundell, K. M., & Goss, W. M. 2007, *MNRAS*, 381, 881
- MAGIC Collaboration, Ahnen, M. L., Ansoldi, S., et al. 2018, *A&A*, 612, A14
- Maloney, P. R., Hollenbach, D. J., & Tielens, A. G. G. M. 1996, *ApJ*, 466, 561
- Margon, B., & Anderson, S. F. 1989, *ApJ*, 347, 448
- Marshall, H. L., Canizares, C. R., Hillwig, T., et al. 2013, *ApJ*, 775, 75
- Moldowan, A., Safi-Harb, S., Fuchs, Y., et al. 2005, *Advances in Space Research*, 35, 1062
- Panferov, A. 2014, *A&A*, 562, A130
- Panferov, A. A. 2017, *A&A*, 599, A77
- Reach, W. T., Rho, J., & Jarrett, T. H. 2005, *ApJ*, 618, 297
- Reynoso, M. M., Romero, G. E., & Christiansen, H. R. 2008, *MNRAS*, 387, 1745
- Rho, J., Hewitt, J. W., Biegging, J., et al. 2017, *ApJ*, 834, 12
- Safi-Harb, S., & Ögelman, H. 1997, *ApJ*, 483, 868
- Safi-Harb, S., & Petre, R. 1999, *ApJ*, 512, 784
- Shan, S. S., Zhu, H., Tian, W. W., et al. 2018, *ApJS*, 238, 35

- Spitzer, L. 1978, Physical processes in the interstellar medium, by Lyman Spitzer. New York Wiley-Interscience, 1978. 333 p.,
- Su, Y., Chen, Y., Yang, J., et al. 2009, ApJ, 694, 376
- Su, Y., Chen, Y., Yang, J., et al. 2011, ApJ, 727, 43
- Su, Y., Zhou, X., Yang, J., et al. 2018, ApJ, 863, 103
- Takayanagi, K. 1973, PASJ, 25, 327
- Tatematsu, K., Fukui, Y., Nakano, M., et al. 1987, A&A, 184, 279
- Turner, B. E., & Gammon, R. H. 1975, ApJ, 198, 71
- Turner, B. E., Chan, K.-W., Green, S., & Lubowich, D. A. 1992, ApJ, 399, 114
- van der Tak, F. F. S., Black, J. H., Schöier, F. L., Jansen, D. J., & van Dishoeck, E. F. 2007, A&A, 468, 627
- Verstraete, L., Pech, C., Moutou, C., et al. 2001, A&A, 372, 981
- Wang, J., & Chen, Y. 2010, Science China Physics, Mechanics, and Astronomy, 53, 271
- Wang, Z.-R., McCray, R., Chen, Y., & Qu, Q.-Y. 1990, A&A, 240, 98
- Wang, Z., Qu, Q., Luo, D., McCray, R., & Mac Low, M.-M. 1992, ApJ, 388, 127
- Watanabe, Y., Sakai, N., Sorai, K., et al. 2014, ApJ, 788, 4
- Watson, M. G., Willingale, R., Grindlay, J. E., et al. 1983, ApJ, 273, 688
- Wilson, T. L., Rohlfs, K., & Hüttemeister, S. 2013, Tools of Radio Astronomy; Astronomy and Astrophysics Library. ISBN 978-3-642-39949-7. Springer-Verlag Berlin Heidelberg, 2013,
- Yamamoto, H., Ito, S., Ishigami, S., et al. 2008, PASJ, 60, 715
- Yamauchi, S., Kawai, N., & Aoki, T. 1994, PASJ, 46, L109
- Yoshiike, S., Fukuda, T., Sano, H., et al. 2013, ApJ, 768, 179
- Zhou, P., & Chen, Y. 2011, ApJ, 743, 4
- Zhou, P., Chen, Y., Safi-Harb, S., et al. 2016, ApJ, 831, 192

Zhou, P., Li, J.-T., Zhang, Z.-Y., et al. 2018, ApJ, 865, 6

Table 1. Observational information of regions N2 and N3 ^a

Region	Line	Frequency (GHz)	Velocity Resolution (km s ⁻¹)
N2	¹² CO($J=1-0$)	115.271	0.508
N2	¹³ CO($J=1-0$)	110.201	0.508
N2	¹² CO($J=2-1$)	230.538	0.254
N2	CN ($J=3/2-1/2$ $F=5/2-3/2$)	113.491	0.508
N3	¹² CO($J=1-0$)	115.271	0.127/0.508
N3	¹³ CO($J=1-0$)	110.201	0.508
N3	¹² CO($J=2-1$)	230.538	0.063/0.254
N3	CN ($J=3/2-1/2$ $F=5/2-3/2$)	113.491	0.508

Note. —

^aThe regions are defined in §2 and delineated in Figure 1.

Table 2. Observed and derived Parameters for the MCs in +50 – +60 km s⁻¹ in Regions N2 and N3 ^a

	N2			N3		
	¹² CO $J=1-0$	¹² CO $J=2-1$	¹³ CO $J=1-0$	¹² CO $J=1-0$	¹² CO $J=2-1$	¹³ CO $J=1-0$
T_{peak} (K)	25.0	22.9	10.4	28.0	26.4	9.2
V_{cent} (km s ⁻¹)	52.7	52.9	52.8	52.1	52.1	52.5
FWHM (km s ⁻¹)	2.6	3.2	2.1	1.7	1.7	1.3
$W(\text{CO})$ (K km s ⁻¹)	70.4	77.6	23.6	49.3	47.3	12.2
$T_{\text{ex}}, T_{c,k}$ (K)	28	28		31	32	
$\tau(^{13}\text{CO})$			0.56			0.34
$N(\text{H}_2)(10^{21}\text{cm}^{-2})^{\text{b}}$			6.7			3.4
$n(\text{H}_2)d_{3,5}(\text{cm}^{-3})^{\text{c}}$			~ 1900			~ 900
$Md_{3,5}^{-2}(10^2 M_{\odot})^{\text{d}}$			~ 4.9			~ 5.0

Note. —

^aThe regions are defined in §2 and delineated in Figure 4.

^bThe averaged column densities within each region.

^cThe averaged densities within each region.

^dThe $N(\text{H}_2)$ masses estimated within each region.

Table 3. Information of CN ($J=3/2-1/2$ $F=5/2-3/2$)

Position	R.A. ^a	Decl. ^a	Size ^b	T_{\max}^c (K)	Line Width ^d (km s ⁻¹)	N(CN) ^e ($\times 10^{14}$ cm ⁻²)	N(H ₂) ($\times 10^{21}$ cm ⁻²)	N(CN)/N(H ₂) ($\times 10^{-8}$)
1	19:09:14.95	05:04:26.0	33'' \times 33''	0.78	1.0	1.7	2.8	6.1
2	19:09:09.80	05:05:21.0	11'' \times 33''	0.48	1.2	1.2	5.5	2.2
3	19:08:54.34	05:05:21.0	33'' \times 22''	0.45	1.4	1.3	3.8	3.4
4	19:09:01.80	05:09:12.0	44'' \times 55''	0.46	1.1	1.1	3.9	2.8
5	19:09:08.33	05:07:55.0	22'' \times 33''	0.45	1.1	1.0	8.3	1.2
6	19:08:02.97	05:03:42.3	11'' \times 33''	0.77	1.6	3.2	19.5	1.6

Note. —

^aThe central positions of the six regions

^bThe CN ($J=3/2-1/2$ $F=5/2-3/2$) emission lines are averaged within these size of regions

^cThe maximum CN ($J=3/2-1/2$ $F=5/2-3/2$) emission brightness temperature in each region

^dThe FWHM of each CN ($J=3/2-1/2$ $F=5/2-3/2$) emission line

^eThe column density of CN is estimated with assumed molecular density of 10^5 cm⁻³ and kinetic temperature of 28 K (N2, position 6) or 31 K (N3, position 1–5).

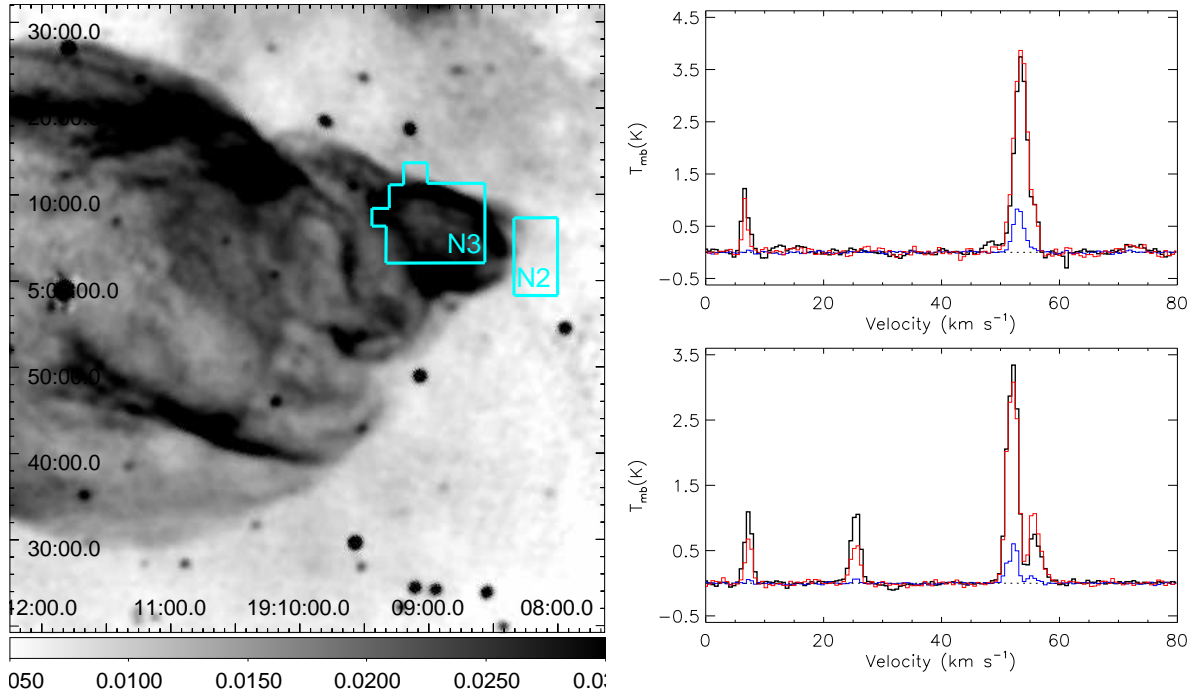


Fig. 1.— (Left) Western part of SNR W50 in radio continuum at 1.4 GHz from Dubner et al. (1998). Regions labeled with “N2” and “N3” delineate the regions we observed with IRAM 30m. (Right) Average CO spectra of regions N2 (right top panel) and N3 (right bottom panel) in the velocity range 0–+80 km s^{−1} from the IRAM observation. The black thick lines are for ¹²CO ($J=1-0$), the blue lines for ¹³CO ($J=1-0$), the red lines for ¹²CO($J=2-1$), and the dotted lines for 0 K main-beam temperature. Note that the ¹²CO ($J=2-1$) is resampled to achieve the same velocity resolution 0.6 km s^{−1} as the ¹²CO ($J=1-0$).

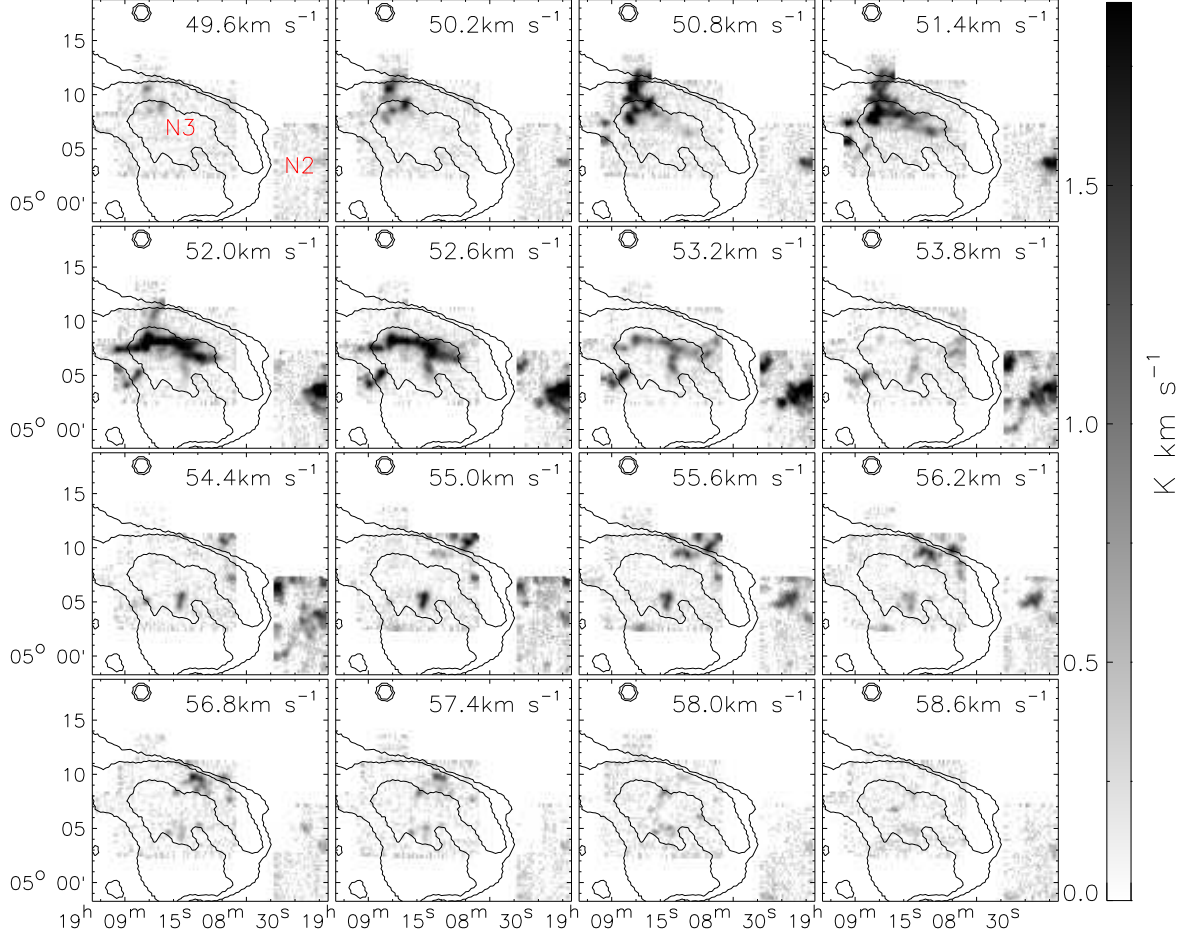


Fig. 2.— IRAM ^{12}CO ($J=1-0$) intensity maps integrated each 0.6 km s^{-1} in velocity range $+49.3 - +58.9 \text{ km s}^{-1}$, overlaid by VLA 1.4 GHz radio contours from Dubner et al. (1998) in black contour. The colorbar shows the square root of the value, and an equatorial coordinate system in J2000 is used. Regions N2 and N3 are labeled in the upper left panel.

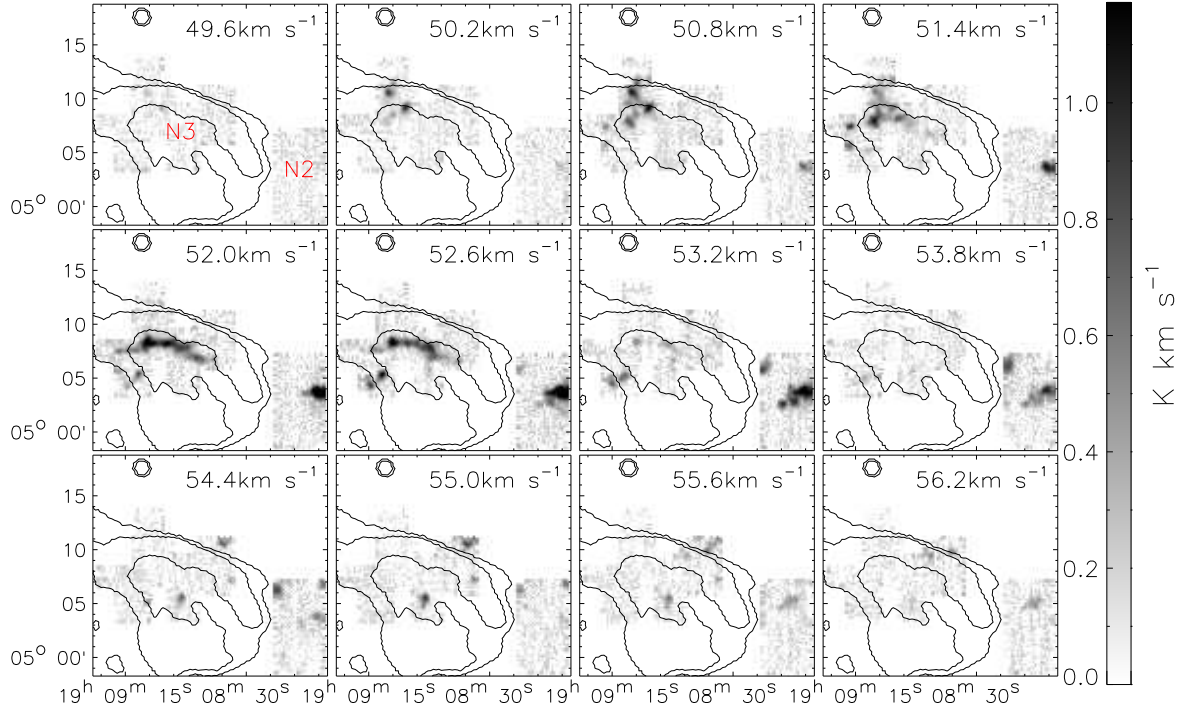


Fig. 3.— IRAM ^{13}CO ($J=1-0$) intensity maps integrated each 0.6 km s^{-1} in velocity range $+49.3 - +56.5 \text{ km s}^{-1}$, overlaid by VLA 1.4 GHz radio contours as the same in Figure 2, and the colorbar shows the square root of the value. Regions N2 and N3 are labeled in the upper left panel.

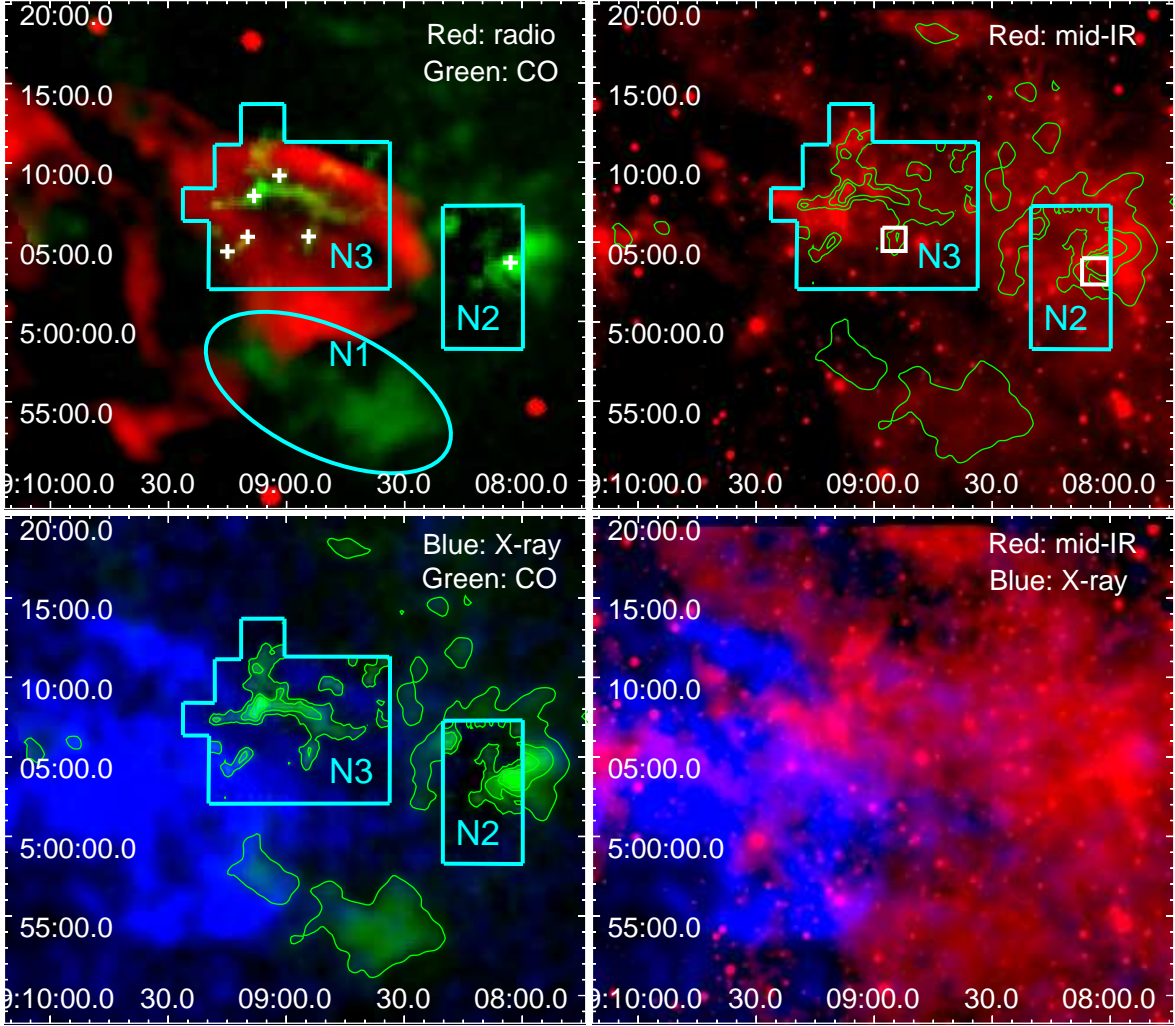


Fig. 4.— Multiwavelength maps of the western lobe of SNR W50: (Upper left) radio continuum at 1.4 GHz from Dubner et al. (1998) is in red, ^{12}CO ($J=1-0$) intensity map integrated in velocity range $+48$ – $+60\text{ km s}^{-1}$ is in green (the data in regions N2 and N3 are from IRAM 30 m, and the data outside the two regions are from PMOD MWISP). The ellipse shows the “SS 433-N1” clump in Yamamoto et al. (2008). The six white crosses mark the project positions where CN lines are detected (see § 3.3). (Upper right) *WISE* $12.082\mu\text{m}$ mid-IR image (with a linear scale) is in red, overlaid with integrated ^{12}CO ($J=1-0$) in $+48$ – $+60\text{ km s}^{-1}$ with levels 10, 20, 30, and 40 K km s^{-1} . Two regions delineated by white rectangles are used to extract CO grid spectra (Figure 5 and 6). (Bottom left) ^{12}CO ($J=1-0$) data shown in green are the same as in the upper left panel. *ROSAT* PSPC $0.5 - 2\text{ keV}$ X-ray emission is in blue. (Bottom right) *WISE* $12.082\mu\text{m}$ mid-IR image (with a square root scale) is in red, and *ROSAT* PSPC $0.5 - 2\text{ keV}$ X-ray emission is in blue (the same as in the bottom left panel).

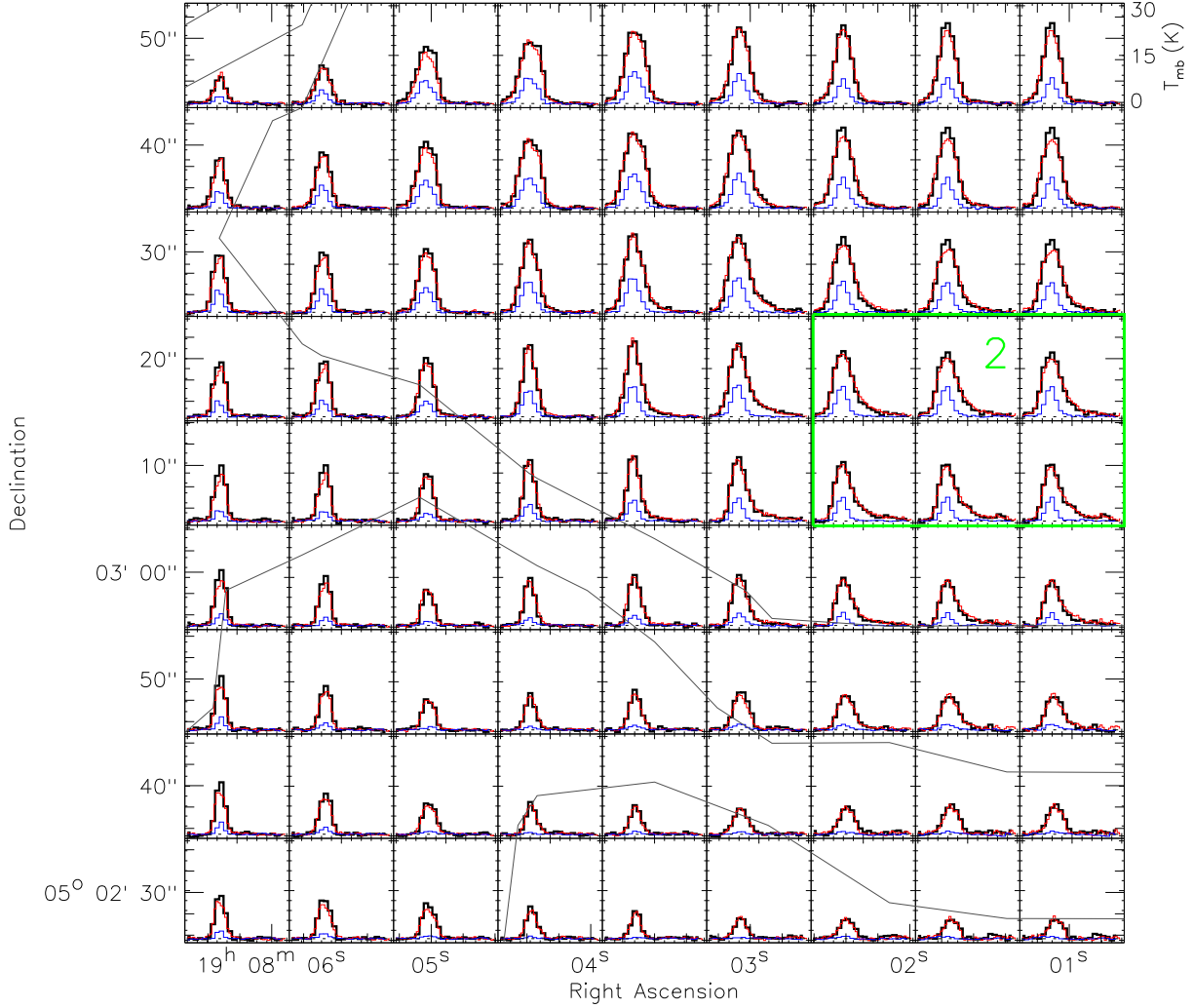


Fig. 5.— Grid of IRAM ^{12}CO ($J=1-0$), ^{12}CO ($J=2-1$), and ^{13}CO ($J=1-0$) spectra in velocity range $+47 - +61 \text{ km s}^{-1}$ for the region delineated by the white rectangle within region N2 in the upper right panel of Figure 4. Black thick lines denote ^{12}CO ($J=1-0$) spectra, red lines denote ^{12}CO ($J=2-1$), blue lines denote ^{13}CO ($J=1-0$), and dashed lines denote the 0 K main-beam temperature. The size of each pixel is $11'' \times 11''$. The contours are the same as in Figure 4.

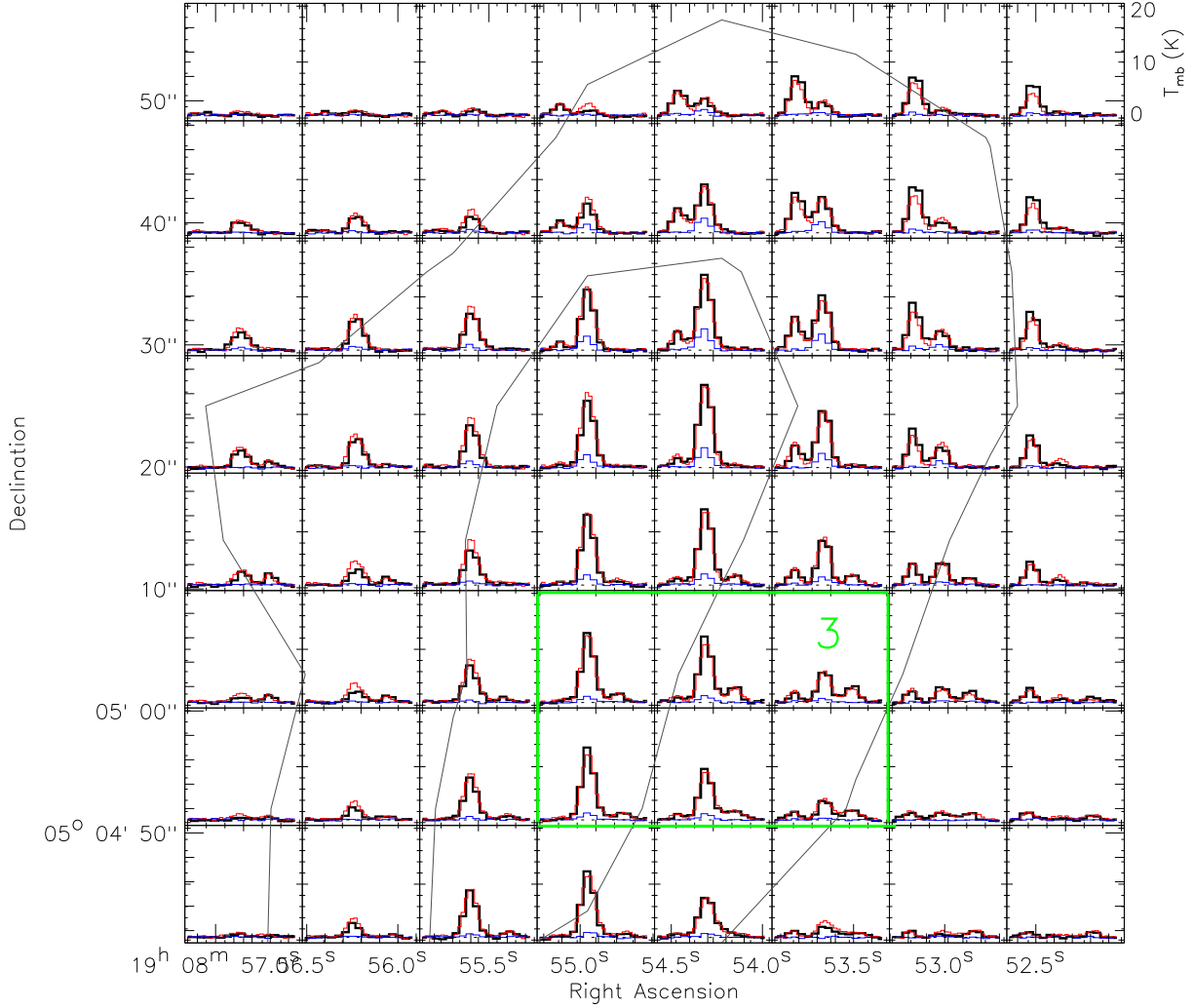


Fig. 6.— Grid of IRAM ^{12}CO ($J=1-0$), ^{12}CO ($J=2-1$), and ^{13}CO ($J=1-0$) spectra in velocity range $+49 - +61 \text{ km s}^{-1}$ for the region delineated by the white rectangle within region N3 in the upper right panel of Figure 4. Black thick, red, blue, and dashed lines denote same spectra as in Figure 5. The size of each pixel is $11'' \times 11''$. The contours are also the same as in Figure 4.

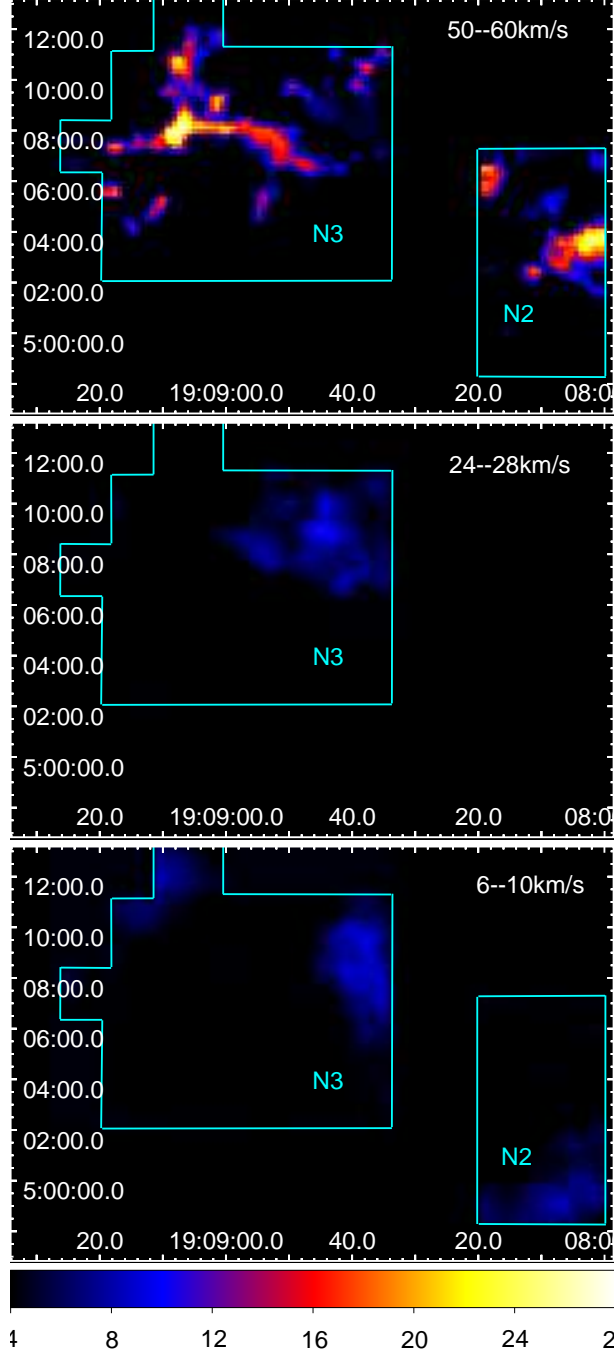


Fig. 7.— Kinetic temperature ($T_{c,k}$) maps of the molecular clumps at velocities $+50 - +60 \text{ km s}^{-1}$ (top panel), $+24 - +28 \text{ km s}^{-1}$ (middle panel), and $+6 - +10 \text{ km s}^{-1}$ (bottom panel) obtained from the IRAM observation, with assumptions that there is no beam dilution ($f = 1$) and $\tau_{12\text{CO}} \gg 1$. Here we have clipped the map where the temperature is lower than 4 K. The cyan regions labeled with “N2” and “N3” are the same as in Figure 1.

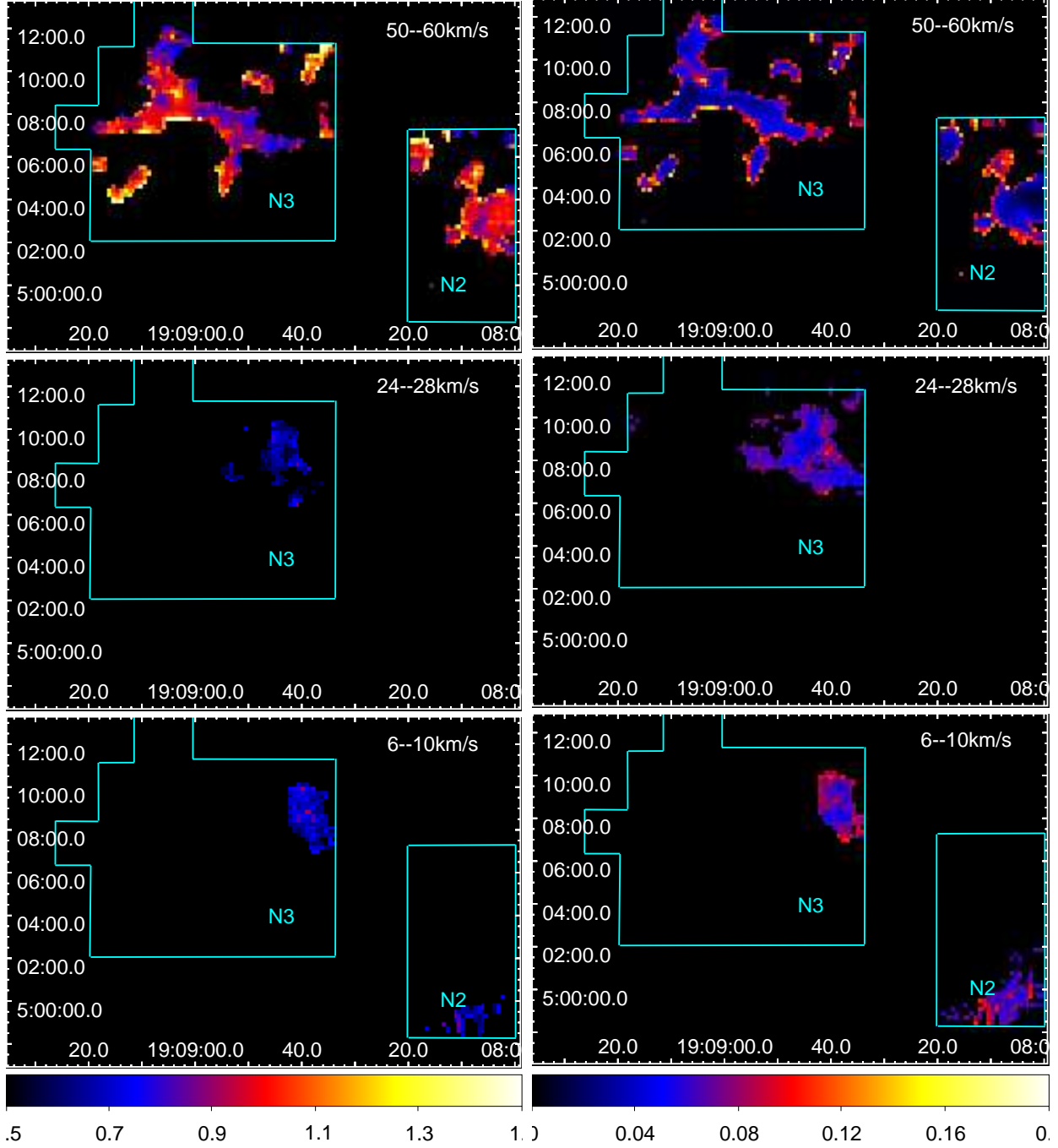


Fig. 8.— IRAM ^{12}CO $J=2-1/J=1-0$ ratio maps for LSR velocity ranges $+50 - +60 \text{ km s}^{-1}$ (top left panel), $+24 - +28 \text{ km s}^{-1}$ (middle left panel), and $+6 - +10 \text{ km s}^{-1}$ (bottom left panel), with the 1σ error maps shown in the right panels, respectively. The cyan regions labeled with “N2” and “N3” are the same as those in Figure 1.

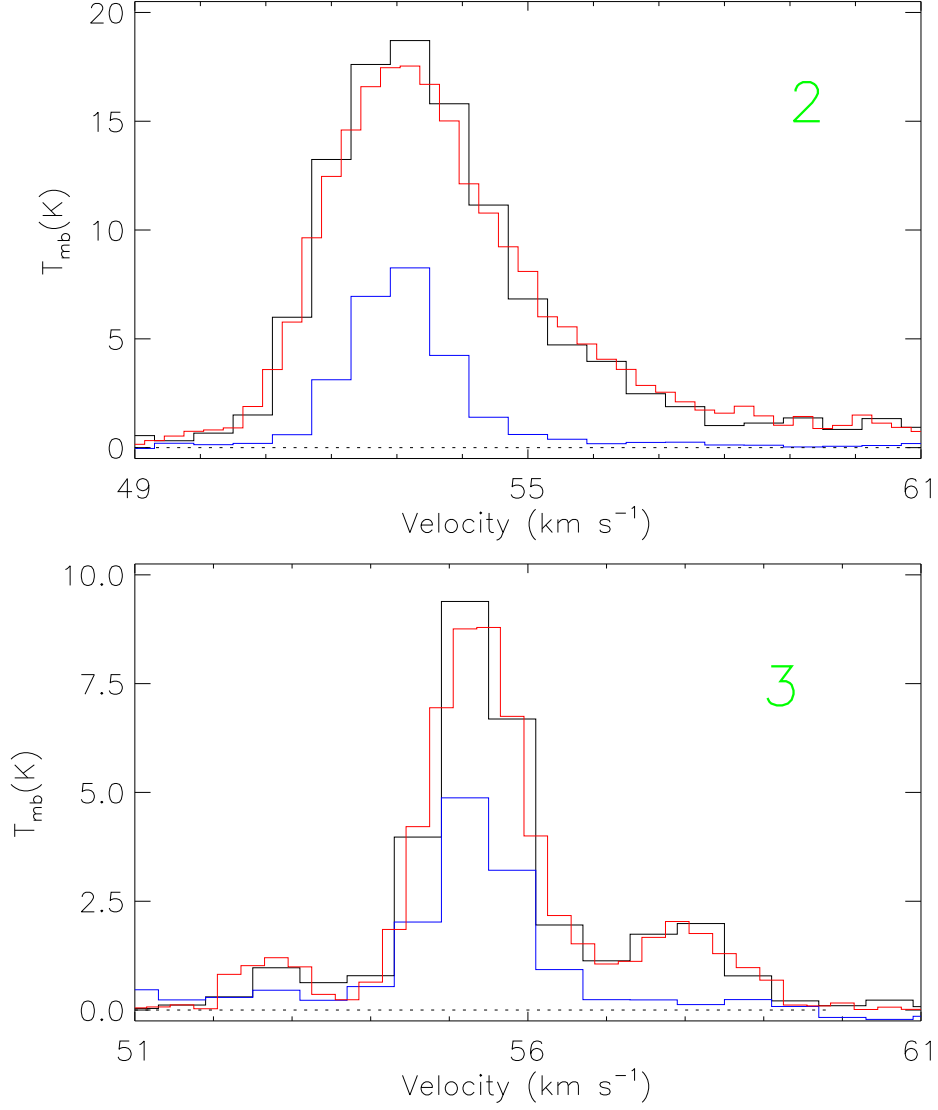


Fig. 9.— Averaged spectra of regions “2” (top panel) and “3” (bottom panel) in the velocity range $+49 - +61 \text{ km s}^{-1}$ and $+51 - +61 \text{ km s}^{-1}$, respectively, obtained from the IRAM observation. The two regions are defined in Figure 5 and 6. The black thick lines denote the ^{12}CO ($J=1-0$) spectra, the red lines represent ^{12}CO ($J=2-1$), the blue lines represent ^{13}CO ($J=1-0$), and the dotted lines represent the 0 K main-beam temperature. The ^{13}CO ($J=1-0$) spectrum in the bottom panel has been multiplied by 5 for better visibility.

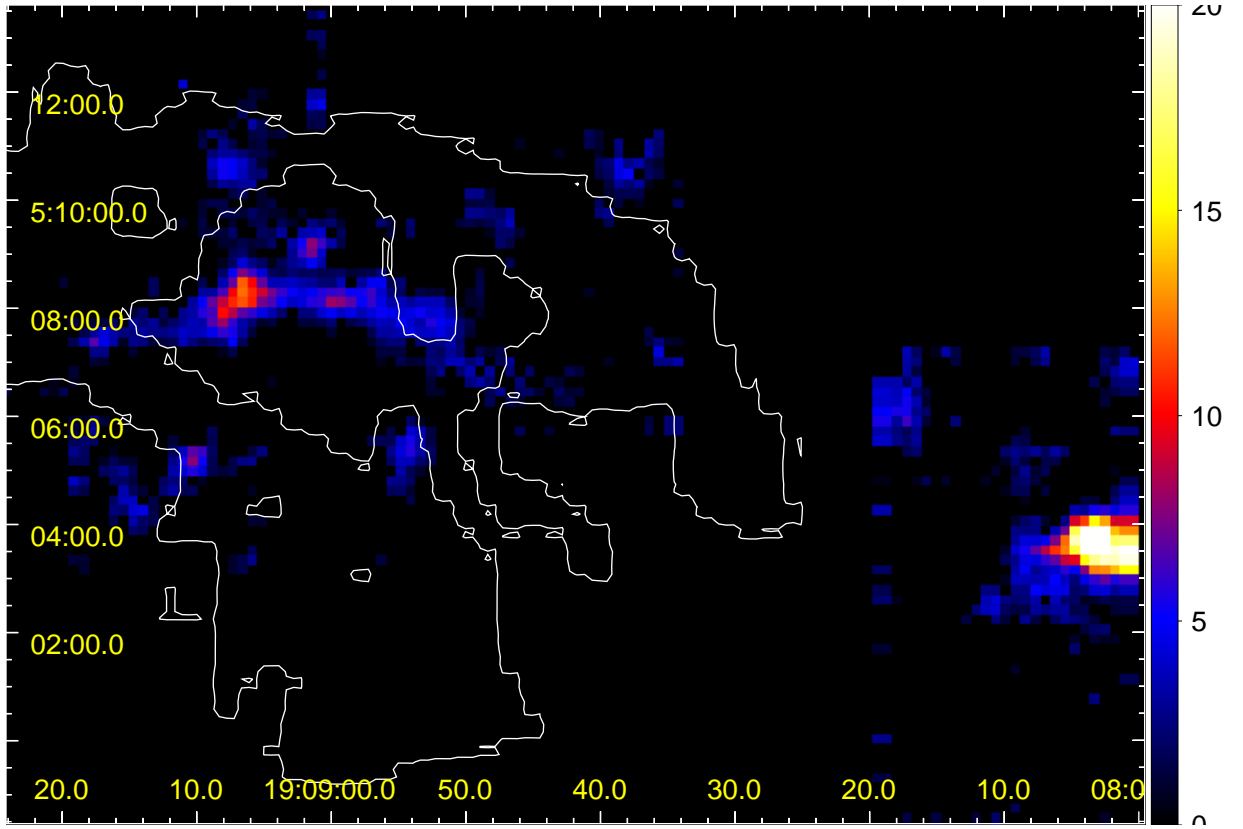


Fig. 10.— $N(\text{H}_2)$ distribution of regions N2 and N3 in the velocity range of $+50 - +60 \text{ km s}^{-1}$ in unit of 10^{21} cm^{-2} obtained from the IRAM observation. The radio contour is the same as in Figure 2.

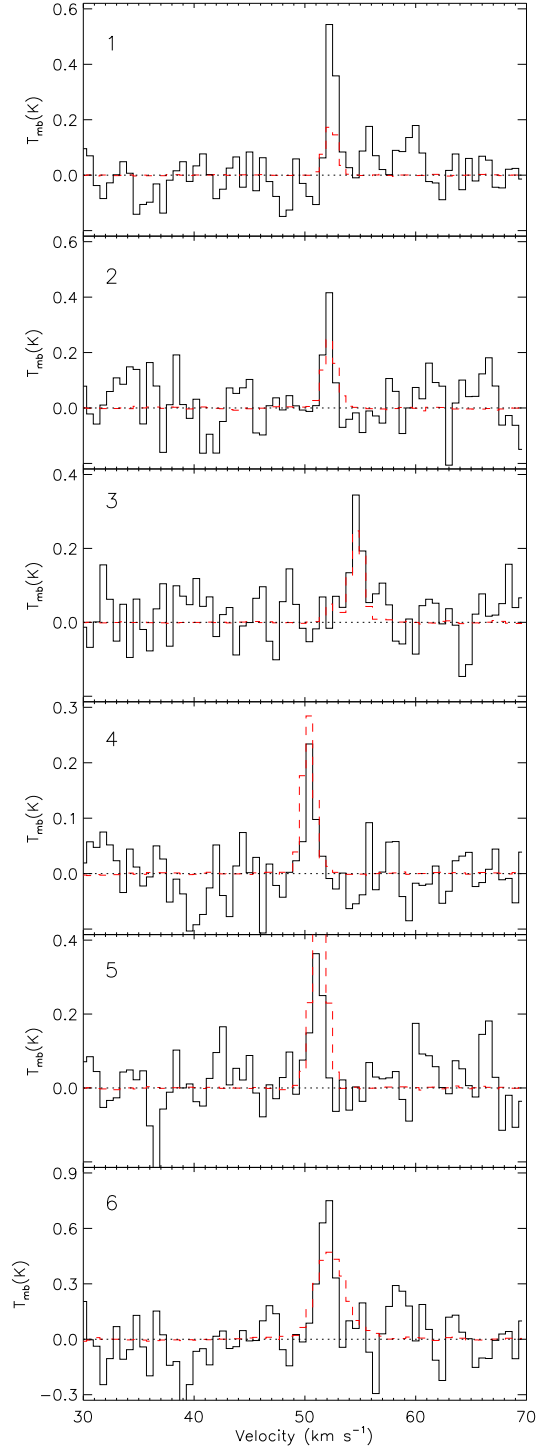


Fig. 11.— IRAM CN ($J=3/2-1/2$ $F=5/2-3/2$) spectra extracted from the regions labeled in the upper left panel of Figure 4, within velocity range $+30 - +70 \text{ km s}^{-1}$. The dotted lines represent the 0 K main-beam temperature. The position information of these regions are summarized in Table 3. As a comparison, ^{12}CO ($J=1-0$) spectra extracted from same regions are also plotted (the red dashed lines, which have been multiplied by a factor of 0.02).

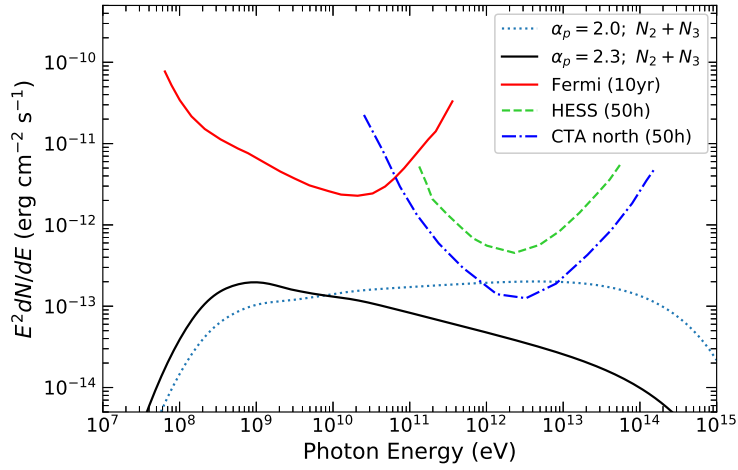


Fig. 12.— Expected gamma-ray fluxes from clumps in regions N2 and N3, with assumed proton indexes of 2.0 (dotted line) and 2.3 (black line). The sensitivity of *Fermi* LAT in 10 yrs (red line, Funk et al. 2013), HESS in 50 hrs (dashed line, di Sciascio & Lhaaso Collaboration 2016), and CTA north in 50 hrs (dash-dotted line, di Sciascio & Lhaaso Collaboration 2016) are overlaid.